Band Bending at CdTe Solar Cell Contacts: Correlating Electro-Optical and X-Ray Photoelectron Spectroscopy Analyses of Thin Film Solar Cells

Darius Kuciauskas, Craig L. Perkins, Marco Nardone, Chungho Lee, Rajni Mallick, and Gang Xiong*

With the semiconductor bulk properties reaching target values for highly efficient solar cells, efforts are applied to reduce losses at solar cell interfaces and contacts. Advances in understanding back contacts in thin-film polycrystalline CdTe solar cells, a leading thin-film PV technology, are reported. By using X-Ray photoelectron spectroscopy, Kelvin probe spectroscopy, time- and energy-resolved photoluminescence, defects at the back contact are analyzed. Densities of recombination centers and charged defects that induce near-back-contact band bending, both resulting in recombination losses, were estimated. Electro-optical and surface analysis results are integrated into a device model, simulating the performance of CdSeTe/CdTe solar cells with 902 mV open circuit voltage.

1. Introduction

Metal or doped semiconductor back contacts (BCs) are commonly used for thin film solar cells. For example, Au, Te, or doped ZnTe BCs are used for CdTe solar cells and Mo BC for CIGS solar cells. Such contacts are optimized to reduce interface barriers for hole transport,[1,2] but they all have high interface recombination velocity S_{back}, typically $S_{back} = 10^5$–10^6 cm s^{-1}.[3,4] As a result, back-contact recombination can limit device voltage. Therefore, selective and passivating contacts need to be developed to increase voltage and efficiency of thin film solar cells.[5] The necessary steps for developing such contacts are understanding band alignment, interface defects, and interface carrier dynamics.

Our focus in this study is BCs in CdTe thin film solar cells. CdTe is the leading thin film photovoltaic (PV) technology, with about 9 GW_{pp} manufactured in 2022 and more than 20 GW_{pp} planned for 2025. For expansion on a larger scale, thin film PV has lower embedded energy and carbon than crystalline PV.[6] Material and device improvements underly successes of CdTe PV technology. As an important benchmark of reducing defect density in polycrystalline absorbers, carrier lifetimes reached >1 μs[7] and external radiative efficiencies $>0.1\%$,[8] both largely due to Se alloying in the CdSeTe absorber.[9] Carrier density can exceed 10^{16} cm^{-3} with group-V doping.[10,11] Change from cation to anion-site doping has also increased reliability.[12] The next focus area is device contacts. Interface recombination velocity was reduced from $>10^5$ to <100 cm s^{-1} with insulating Al_2O_3,[13] which is a proof of concept for improved polycrystalline interfaces and contacts, but these results have not yet been transferred to device fabrication. It is widely recognized that recombination losses in thin film solar cells can be attributed to Shockley–Read–Hall (SRH) recombination in the absorber bulk and near device contacts.[5] In this study, we develop methodology to differentiate losses due to interface defects and interface charges.

To understand CdTe BCs, we analyze device stacks 1–4 in **Scheme 1**. These stacks include hole transport layer (HTL) applied between the absorber (CdTe) and the BC.[14] In perovskite PV, HTL is a key part of device architecture, and we investigate organic poly(triaryl) amine (PTAA) as HTL in CdTe solar cells. Comparison is made between non-passivated absorber stack (sample 1), stack with HTL (sample 2),[14] ZnTe contacts (sample 3, this contact is used in state-of-the-art CdTe devices),[10,15] and HTL/ZnTe contacts (sample 4). Incomplete device stacks 1–4 are partially transparent from the back side, enabling electro-optical (EO) and surface analysis characterization. Metal stack is applied to sample 4 to fabricate complete device for which current voltage (JV) and external quantum efficiency (EQE) can be measured. Device performance is shown in Section 4.

To evaluate the impact of interface charges and interface defects, we combine surface analysis (X-ray photoelectron spectroscopy (XPS) and Kelvin probe spectroscopy) and

D. Kuciauskas, C. L. Perkins
Materials, Chemical, and Computational Science Directorate
National Renewable Energy Laboratory
Golden, CO 80401, USA
E-mail: Darius.Kuciauskas@nrel.gov

M. Nardone
Department of Physics and Astronomy
Bowling Green State University
Bowling Green, OH 43403, USA

C. Lee, R. Mallick, G. Xiong
California Advanced Research
First Solar
Santa Clara, CA 95050, USA

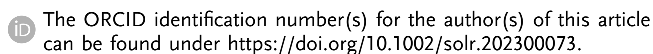
The ORCID identification number(s) for the author(s) of this article can be found under https://doi.org/10.1002/solr.202300073.

© 2023 The Authors. Solar RRL published by Wiley-VCH GmbH. This is an open access article under the terms of the Creative Commons Attribution-NonCommercial License, which permits use, distribution and reproduction in any medium, provided the original work is properly cited and is not used for commercial purposes.

DOI: 10.1002/solr.202300073

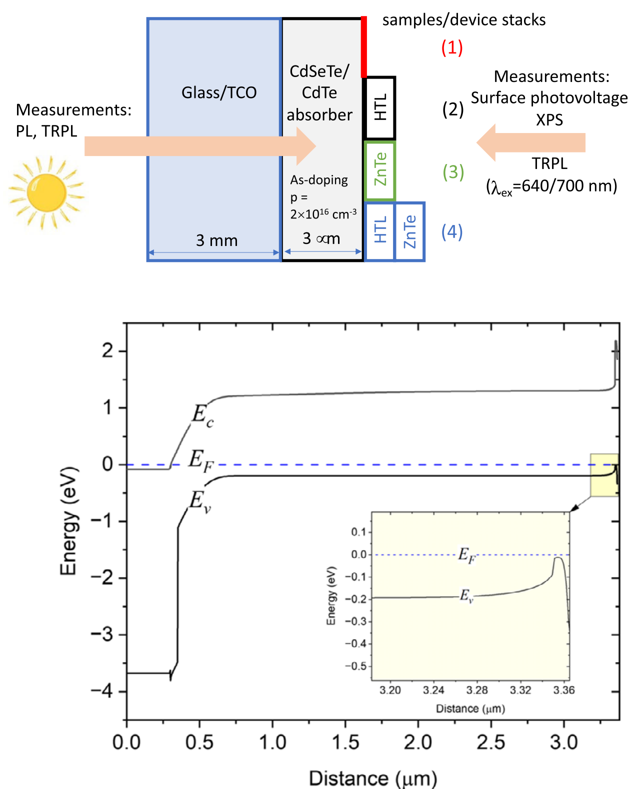

Scheme 1. Samples and measurements in this study and band diagram of solar cell device. Color code (red/black/green/blue) is used in Figure 1, 3, and 5 to identify samples 1–4.

photoluminescence (PL) characterization. Because XPS, Kelvin probe, and PL have different probing resolutions, results are integrated using solar cell device models, including modeling of charge carrier dynamics after pulsed laser excitation in the solar cell device.

2. Results and Discussion

2.1. PL Emission Spectra, Radiative Voltage, and Charge Carrier Lifetimes

In **Figure 1**, we analyze the impact of HTL and/or ZnTe BC layers on radiative efficiency and carrier lifetimes. Measurements are taken from the substrate (glass) side, which is the direction illuminated by the Sun in solar cells. Figure 1a shows absolute PL emission spectra at 1 Sun equivalent photon fluence of 1.98×10^{21} photons $(\text{cm}^2\ \text{s})^{-1}$. The emission maximum is at 1.28 eV, which is substantially below the bandgap of the absorber ($E_g = 1.40$ eV). The emission spectrum is broad and distinctly different from PL emission of Cu-doped CdTe solar cells.[16,17] Such spectral features are introduced by As dopants[18] and indicate electrostatic potential fluctuations.[19] In comparison to the absorber without passivation (sample 1), emission intensity is higher for sample 2 with HTL. Emission intensity is reduced (PL emission quantum yield PLQY decreases ≈10 times) with ZnTe (sample 3) and HTL/ZnTe (sample 4). Emission is somewhat stronger with HTL/ZnTe (sample 4) than with ZnTe (sample 3). Especially for samples 3 and 4 with reduced *PLQY*, spectra are affected by above-E_g signal with the maximum at ≈1.5 eV. Control experiments with glass substrates showed that this signal is due to glass. This artifact in the PL emission data is shown as the shaded spectrum in Figure 1a.

The impact of interface recombination can be inferred from the exponents u of integrated PL emission intensity versus excitation fluence, $I_{PL} \propto (\text{excitation})^u$.[20] Exponents u are also called optical diode factors,[20] and their values for the 0.12–1 Suns excitation range are given in the inset of Figure 1a. The $u = 1.80 \pm 0.02$ for samples 1 and 2 indicate large impact of interface recombination and the application of HTL does not change this result. Data for samples 3 and 4 is ambiguous because of the lower PLQY and resulting larger impact of above-E_g emission artifact ($u = 1$ for glass).

High-energy emission shoulder due to glass makes spectral fitting to determine implied voltage (also called quasi-Fermi level splitting $\Delta\mu$) uncertain.[21] Despite these limitations, it is important to estimate radiative voltage V_{OC}^{rad}, because V_{OC}^{rad} sets the thermodynamic limit for the solar cell voltage. To determine V_{OC}^{rad}, we calculated absorptance spectra $a(E)$ from the generalized Planck's Law

$$I_{PL}(E) = \frac{2\pi\varepsilon^2}{h^3c^2}a(E)\frac{1}{exp(\frac{E-\Delta\mu}{k_BT}) - 1} \quad (1)$$

where $I_{PL}(E)$ is PL emission intensity (units photons $\text{eV}^{-1}\ \text{m}^{-2}\ \text{s}^{-1}$), E is energy, h is Planck's constant, c is speed of light, k_B is Boltzmann's constant, and T is temperature. To calculate $a(E)$ from Equation (1), we need to know $\Delta\mu$ and T. Onno et al. reported that for similar As-doped devices voltage is close to $\Delta\mu$.[18] Therefore, we used $\Delta\mu = 850$ mV, which is typical device voltage, and $T = 297$ K. The absorptance calculated using Equation (1) and shown in Figure 1b is normalized to $a(1.5\ \text{eV}) = 1$. Such normalization is used because 0.1 eV above the bandgap (at 1.5 eV, $E_g = 1.4$ eV) excitation is nearly completely absorbed in the CdSeTe semiconductor layer.

With these assumptions ($\Delta\mu = 850$ mV, $T = 297$ K, and $a(1.5\ \text{eV}) = 1$) absorptance is determined over many orders of magnitude, which is a consequence of PL emission spanning the spectral range down to 0.8 eV. Such data indicates the presence of the band tails. In comparison to other PV absorbers,[22] band tails are relatively large. This aspect will be investigated in the future using simpler samples because device stacks in Scheme 1 are graded in bandgap, recombination lifetime, and other properties,[10] potentially including bandtails.[19]

To quantify band tails using the Urbach model, we consider absorptance at <1.2 eV, where data is not changed by the high energy emission shoulder. Absorptance spectra for samples 1–3 can be described by the Urbach energy $E_u = 23$–24 meV and slightly higher $E_u = 26$ meV for sample 4. This small apparent E_u increase for sample 4 is a consequence of higher PL amplitude at <1.2 eV (compare green and blue spectra in Figure 1a) and can be attributed to improved cell optics, rather than increased defect density.[18,23]

© 2023 The Authors. Solar RRL published by Wiley-VCH GmbH

2367198x, 2023, 10, Downloaded from https://onlinelibrary.wiley.com/doi/10.1002/solr.202300073 by National Renewable Energy Lab, Wiley Online Library on [01/06/2023]. See the Terms and Conditions (https://onlinelibrary.wiley.com/terms-and-conditions) on Wiley Online Library for rules of use; OA articles are governed by the applicable Creative Commons License

2367198x, 2023, 10, Downloaded from https://onlinelibrary.wiley.com/doi/10.1002/solr.202300073 by National Renewable Energy Lab, Wiley Online Library on [01/06/2023]. See the Terms and Conditions (https://onlinelibrary.wiley.com/terms-and-conditions) on Wiley Online Library for rules of use; OA articles are governed by the applicable Creative Commons License

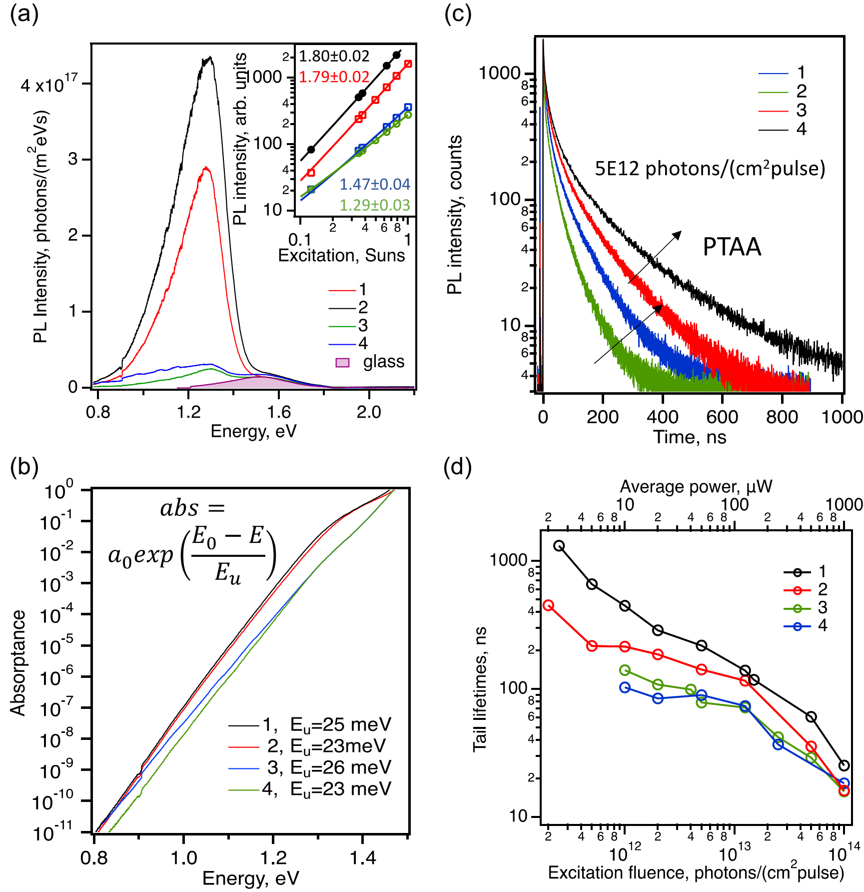

Figure 1. a,b) PL and c,d) TRPL characterization of device stacks listed in Scheme 1 when measurements are taken through glass substrate. a) Absolute PL emission spectra and integrated PL emission intensity versus excitation fluence (inset, with power-law exponents u for each sample). b) Absorptance spectra calculated from PL data in A. Inset gives formula used to fit Urbach energy E_u and E_u values for each sample. c) TRPL decays (excitation 640 nm, fluence 5×10^{12} photons $(\text{cm}^2\text{pulse})^{-1}$). d) TRPL tail lifetimes versus excitation fluence (bottom axis) and excitation power (upper axis).

We calculated V_{OC}^{rad} from the absorptance spectra $a(E)$

$$V_{OC}^{rad} = \frac{k_B T}{q} \ln\left(\frac{J_{SC}}{J_0^{rad}} + 1\right) = \frac{k_B T}{q} \ln\left(\frac{q \int_0^\infty a(E)\phi_{Sun}(E) dE}{q \int_0^\infty a(E)\phi_{bb}(E) dE} + 1\right) \quad (2)$$

where q is elementary charge, J_{SC} is short-circuit current density, J_0^{rad} is radiative saturation-current density, $\phi_{Sun}(E)$ is the solar spectrum, and $\phi_{bb}(E)$ is the black body spectrum. Using absorptance in Figure 1b and Equation (2), $V_{OC}^{rad} = 1017$–1057 mV. This range is in good agreement with V_{OC}^{rad} for similar As-doped absorbers where $a(E)$was estimated from the EQE spectra.[18] Therefore, As-doped absorber stacks in this study can produce voltages larger than 1 V. Voltages $V_{OC} = 850$–900 mV are typical in devices, suggesting large impact of recombination.

Next, we examine recombination dynamics from the glass-side TRPL data (Figure 1c,d). Modeling for *p*-n junction devices after pulsed laser excitation supports using exponential fit to the tail of the TRPL decay to estimate total recombination rate[24]

$$\frac{1}{\tau_{TRPL}} = \frac{1}{\tau_B} + \frac{1}{\tau_{front}} + \frac{1}{\tau_{back}} + \frac{1}{\tau_{radiative}} \quad (3)$$

where $\tau_{TRPL}$is exponential lifetime of the tail of the TRPL decay, $\tau_B$is SRH recombination lifetime due to recombination in the bulk, τ_{front} and τ_{back} are SRH lifetimes due to recombination near front and BCs, $\tau_{radiative} = 1/(Bp)$ is radiative lifetime, B is radiative recombination coefficient, and p is doping. The four terms in Equation (3) describe bulk, front, back, and radiative recombination rates.

Lowest fluence ($<10^{12}$ photons/(cm^2 pulse)) lifetimes τ_{TRPL} are longer, up to >1 µs for HTL stack 2, possibly due to "charge storage effect" in the device.[24] The lifetimes at $>10^{13}$ photons/(cm^2 pulse) are shorter due to increased radiative recombination at high injection. The middle range of injection, $\approx 10^{12}$–10^{13} photons $(\text{cm}^2\text{pulse})^{-1}$, establishes conditions to evaluate bulk and interface recombination and is used to compare samples 1–4. As shown in Figure 1c, decays at this fluence are substantially different, which is attributed to BC recombination—bulk and front interfaces in device stacks 1–4 are expected to be the same.

Comparing τ_{TRPL} for 1 and 2 indicates increased $\Delta \frac{1}{\tau_{TRPL}} \approx \Delta \frac{1}{\tau_{back}} = 2.5 \times 10^6\ \text{s}^{-1}$ without HTL. Lifetimes τ_{TRPL} for samples 3 and 4 indicate similar increase in BC recombination rate by $\Delta \frac{1}{\tau_{back}} \approx 1.6 \times 10^6\ \text{s}^{-1}$. HTL does mitigate some recombination;

© 2023 The Authors. Solar RRL published by Wiley-VCH GmbH

compare blue/green and red/black TRPL decay kinetics in Figure 1c.

Simulations using TRPL modeling code developed by Moseley et al.[24,25] showed that glass-side TRPL data is more sensitive to the defect density near BC than to the BC band bending. In addition, glass-side TRPL decays are impacted by charge carrier mobility and diffusion coefficient, because recombination near BC occurs after carriers diffuse through 3-μm-thick absorber (Scheme 1). Thus, to distinguish the impact of BC interface charges versus BC interface defects glass-side TRPL measurements are not sufficient, and this aspect is better addressed with back-side lifetimes measurements and modeling (Section 2.3 and 2.4).

Overall, data in Figure 1 indicates that BC recombination significantly impacts solar cell performance, including increased recombination losses by about 60 mV (PLQY reduced by ≈10× for samples 3 and 4 vs samples 1 and 2). Our goal is to understand origin of these losses. For this, we use direct band bending measurements with XPS and Kelvin probe, back-side recombination lifetime analysis, and device modeling.

2.2. Band Positions

Band positions of the device stacks in Scheme 1 were determined using XPS and Kelvin probe-based surface photovoltage (SPV) measurements. We first discuss XPS results. As a first step, clean CdTe and ZnTe surfaces were prepared in-situ via sputtering with a gas cluster ion source (15 kV Ar_{2000}^{+}). Wide-range survey spectra (Figure S1, Supporting Information) of both films showed only the expected peaks for cadmium, tellurium, and zinc. X-ray excited valence band spectra of ZnTe were compared with theoretical total density of states (DOS) broadened by a Gaussian function with width (0.18 eV) determined from a comparison of the 0 eV Fermi edge feature of clean gold foil and the Fermi function E_F at 298 K (Figure S2, Supporting Information). Because the XPS energy scale is calibrated to have $E_F = 0$ eV and the theoretical DOS has a scale such that the valence band maximum (VBM) is set to 0 eV, the energy shift necessary to bring the broadened DOS edge in agreement with the XPS valence band onset is equal to the $E_{VBM} - E_F$. The value $E_F - E_{VBM} = 0.44$ eV determined from this procedure agrees well with the simpler method of extrapolating the linear portion of the valence band edge down to the energy axis as has been observed for other materials.[26] Previously we showed that for CdTe the two VBM localization methods agree well,[27] and for this work, CdTe VBMs were located by the linear extrapolation method.

Figure 2 shows core level and valence band spectra from the cleaned reference CdTe (panel a) and ZnTe (panel b) films. Transition energies are shown in electron volts. From these data, core level to VBM energies in the reference materials were determined (Table S1, Supporting Information). Core-level spectra were then used to locate the CdTe valence bands in the device stacks of interest. In **Figure 3** are high energy resolution spectra of the four film stacks: Te $3d_{5/2}$ spectra of films without ZnTe in panel a, Cd $3d_{5/2}$ spectra for all films in panel b, and Zn $2p_{3/2}$ spectra from films with ZnTe in panel c.

Panel (a) in Figure 3 omits Te $3d_{5/2}$ spectra from film stacks with ZnTe to highlight band positionsin the CdTe absorber.

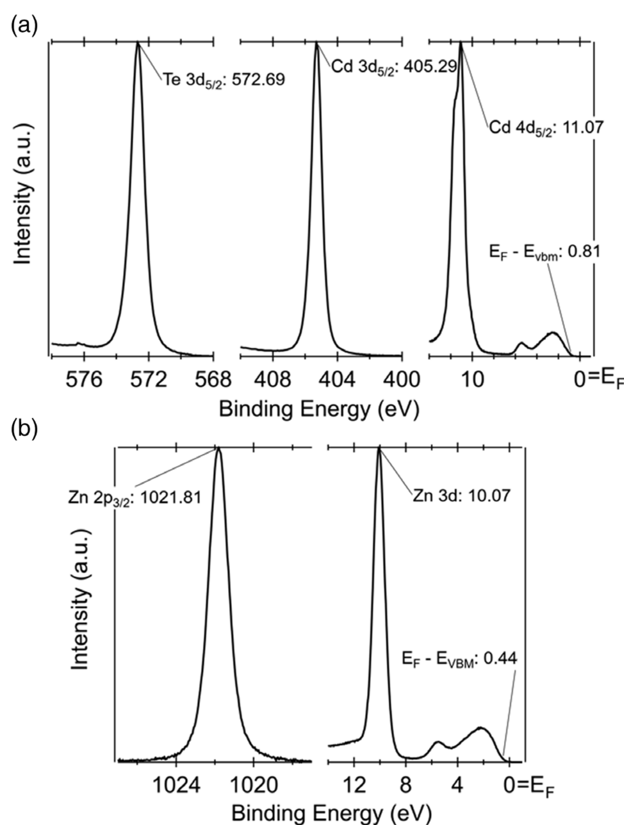

Figure 2. a) $3d_{5/2}$ and valence band spectra from clean CdTe. b) Spectra of the $2p_{3/2}$ and valence band regions of clean ZnTe. Numbers within graphs are transition energies in electron volts.

The spectra show two chemical states for tellurium that correspond to Te^{4+} in the CdTe native oxide and Te^{2-} in the CdTe lattice. The Te^{4+} component was ignored in the following analysis of CdTe band positions. Inspection of the Te^{2-} chemical components indicates that HTL had only a small effect on the band positions at the absorber layer underneath the $CdTeO_x$ native oxide, with the HTL on film 2 inducing about another 0.1 eV of downward band bending relative to film 1 without HTL (**Table 1**).

In Figure 3b, raw Cd $3d_{5/2}$ spectra from device stacks with ZnTe BCs (films 3, 4) were much lower in intensity due to attenuation from the ZnTe layer; all spectra have been normalized in height. These spectra allow assessment of CdTe band positions in all four films since cadmium is not present in the ZnTe layer. Immediately apparent is that growth of ZnTe causes a large ≈0.3 eV reduction in the downward band bending in comparison to the free surface of the CdTe absorber (Table 1). The 0.1 eV increase in downward band bending caused by HTL in the ZnTe-free films 1 and 2 and seen in the Te $3d_{5/2}$ spectra is also observed in these Cd $3d_{5/2}$ spectra. In contrast, HTL sandwiched between the absorber and ZnTe layers has little effect on the CdTe positions as seen in the near overlap of spectra from films 3 and 4.

Panel c of Figure 3 is comprised of the Zn $2p_{3/2}$ spectra used to locate the ZnTe valence band maxima in the two film stacks 3 and 4. As evidenced by the near overlap of these spectra, the

 © 2023 The Authors. Solar RRL published by Wiley-VCH GmbH

2367198x, 2023, 10, Downloaded from https://onlinelibrary.wiley.com/doi/10.1002/solr.202300073 by National Renewable Energy Lab, Wiley Online Library on [01/06/2023]. See the Terms and Conditions (https://onlinelibrary.wiley.com/terms-and-conditions) on Wiley Online Library for rules of use; OA articles are governed by the applicable Creative Commons License

2367198x, 2023, 10, Downloaded from https://onlinelibrary.wiley.com/doi/10.1002/solr.202300073 by National Renewable Energy Lab, Wiley Online Library on [01/06/2023]. See the Terms and Conditions (https://onlinelibrary.wiley.com/terms-and-conditions) on Wiley Online Library for rules of use; OA articles are governed by the applicable Creative Commons License

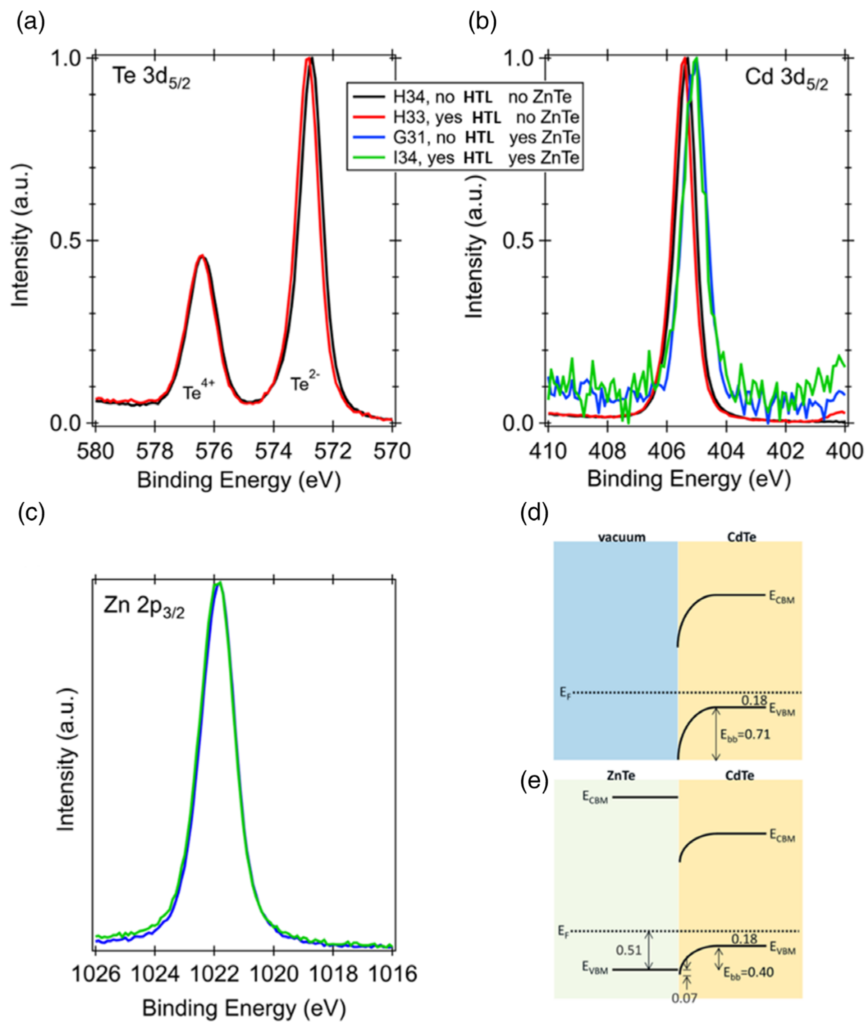

Figure 3. High-resolution XPS data and band diagrams summarizing results. a) Te $3d_{5/2}$ spectra from the two film stacks without ZnTe. b) Cd $3d_{5/2}$ spectra for all four film stacks. c) Zn $2p_{3/2}$ spectra from film stacks 3 (G31) and 4 (I34) that had ZnTe back contacts. d,e) show absorber and ZnTe band positions for the HTL-free case.

Table 1. XPS and Kelvin probe results quantifying band positions at the back contact.

Sample	BC stack	CdTe surface band positions, [eV]		ZnTe surface band positions, [eV]	Kelvin probe	
		E_F-E_{VBM} from Cd $3d_{5/2}$	E_F-E_{VBM} from Te $3d_{5/2}$	E_F-E_{VBM} from Zn $2p_{3/2}$	Surface work functions [eV]	Surface band bending [eV]
1 (H34)	–	0.89	0.86	n/a	4.81	0.81
2 (H33)	HTL	0.99	0.97	n/a	4.73	0.89
3 (G31)	ZnTe	0.59	n/a	0.51	n/a	n/a
4 (I34)	HTL/ZnTe	0.62	n/a	0.54	n/a	n/a

presence of HTL had little effect on ZnTe band positions. Surface band positions for the HTL-free CdTe and CdTe/ZnTe film stacks summarized in Table 1 and shown in Figure 3d,e were derived from these XPS results along with knowledge of the bulk Fermi level obtained from capacitance–voltage (CV). Consistent with prior reports[28] there is a minimal 70 meV barrier between the CdTe and ZnTe valence bands. However, there appears to be a substantial ≈0.5 eV BC barrier due solely to ZnTe, also observed in prior investigations.[28]

Injection-dependent lifetime measurements agree with this estimate ($\mu\varphi_{bi}$ product is estimated in lifetime analysis, where μ is mobility and φ_{bi} is built-in voltage, Section 2.3), while device modeling shows that barrier ≤0.35 eV (Section 2.4). There are at least three possible reasons for this discrepancy: 1) metallization

© 2023 The Authors. Solar RRL published by Wiley-VCH GmbH

2367198x, 2023, 10, Downloaded from https://onlinelibrary.wiley.com/doi/10.1002/solr.202300073 by National Renewable Energy Lab, Wiley Online Library on [01/06/2023]. See the Terms and Conditions (https://onlinelibrary.wiley.com/terms-and-conditions) on Wiley Online Library for rules of use; OA articles are governed by the applicable Creative Commons License

of the ZnTe surface and subsequent formation of a ZnTe/metal interface is likely to substantially change the ZnTe band position relative to the native oxide-covered surface studied here and 2) as noted by Klein, area-averaging characterization techniques such as XPS and PL can produce results inconsistent with transport measurements if transport (and band alignments) is laterally nonuniform.[29] We note that Späth et al. cited tunneling as the mechanism responsible for good transport in ZnTe/metal junctions that had been measured by XPS to have a 0.5 eV barrier.[28] Finally, 3) XPS results were obtained on films that had not been light soaked at elevated temperature, a procedure that tends to reduce downward band bending by about 0.1 eV as shown in **Figure 4** from Kelvin probe data.

Figure 4 summarizes Kelvin probe-determined band bending and work functions through stages of device processing. The initial band bending and surface work function of $CdCl_2$ treated absorber surface are 0.81 and 4.81 eV, respectively. HTL coating and bake degrade the surface band bending to 0.89 eV. Light soak under 1 Sun at an elevated temperature could recover and reduce band bending to 0.74 eV. Since the absorber interfaces with BC layer, ZnTe, the pertinent band bending is the interface band bending instead of the surface band bending. However, Kelvin probe measurement is limited to the exposed surface. Based on XPS, ZnTe layer interface could improve the absorber band bending by 0.33 eV. The absorber interface band bending with ZnTe and at postlight soak is estimated to be 0.41 eV.

In summary, Table 1 shows band positions measured by XPS and Kelvin probe. When both measurements are possible (samples 1 and 2), results are in good agreement.

2.3. Initial Rate Analysis for BC Recombination

To understand the impact of band bending on carrier dynamics, we used back-side TRPL measurements with excitation at 640 and 770 nm. This allows probing within the depletion region (depletion width $w_d \approx 0.2$ μm for 10^{16} cm^{-3} doping and absorption depth $1/\alpha_{640} \approx 75$ nm, where $\alpha_{640\,\text{nm}}$ is absorption coefficient at 640 nm) and at a greater depth ($1/\alpha_{770} \approx 150$ μm). Photogenerated carriers can drift and diffuse, and analysis needs to include modeling of charge carrier transport (Section 2.4). But on the short time scale (≤1 ns is used in **Figure 5**) luminescence is emitted from the well-defined photogeneration region and initial drift and recombination rates can be quantified using an analytical model. Data in Figure 5 is analyzed using the initial rate model that includes drift, interface recombination, diffusion, and radiative recombination rates

$$\frac{1}{\tau_1} = \frac{\alpha \mu E}{2} + \frac{1}{\tau_{\text{back}}} + \frac{k_B T}{q}\alpha^2 \mu + \frac{1}{\tau_{\text{radiative}}} \tag{4}$$

where τ_1 is initial TRPL lifetime from the fit on the 0–1 ns time scale (deconvolution of the instrumental response was used to determine τ_1), μ is charge carrier mobility, and E is strength of the near-interface space charge field. Rate $\tau_{\text{back}}{}^{-1}$ describes SRH recombination near BC, while the first term describes drift due to charged interface defects. In comparison to Equation (3), initial rate model does not include bulk recombination (bulk lifetimes are much longer, Figure 1). Front interface recombination rate is also not included, because after back-side excitation carriers do not reach front contact on the ≤1 ns time scale.

Drift can be distinguished from injection-dependent measurements, and injection is varied by 5–6 orders of magnitude in the data in Figure 5c,d. The radiative recombination dominates at fluence $>10^{15}$ photons (cm^{2}pulse)$^{-1}$ and is clearly distinguishable from reduced lifetimes at the highest fluence range. Diffusion rate $\frac{k_B T}{q}\alpha^2 \mu$ is smaller relative to other contributions, and it can also be added to the SRH recombination rate ($\tau_{\text{back}}{}^{-1}$) because in the first approximation diffusion and recombination rates are independent of injection. The interface recombination term can be written as $\tau_{\text{back}}{}^{-1} = 2\alpha S_{\text{back}}$, where S_{back} is interface recombination velocity.

In addition to the linear response model in the drift term in Equation (4) ($\tau_{\text{drift}}^{-1} = \alpha \mu E/2$), more complex expressions were used.[30–32] Such expressions apply when electrical bias is applied to the solar cell,[30] or when charge carrier diffusion length is high.[32] For example, by solving the continuity equations for solar cell with applied bias, Maiberg et al. derived $\tau_{\text{drift}}^{-1} = \frac{\mu^2}{4D}E^2$, where D is diffusion coefficient for minority carriers.[30] For PL measurements with constant wave (not pulsed) excitation, Cadiz et al. started with the exponential dependence of the dark current on the surface barrier height and found that the

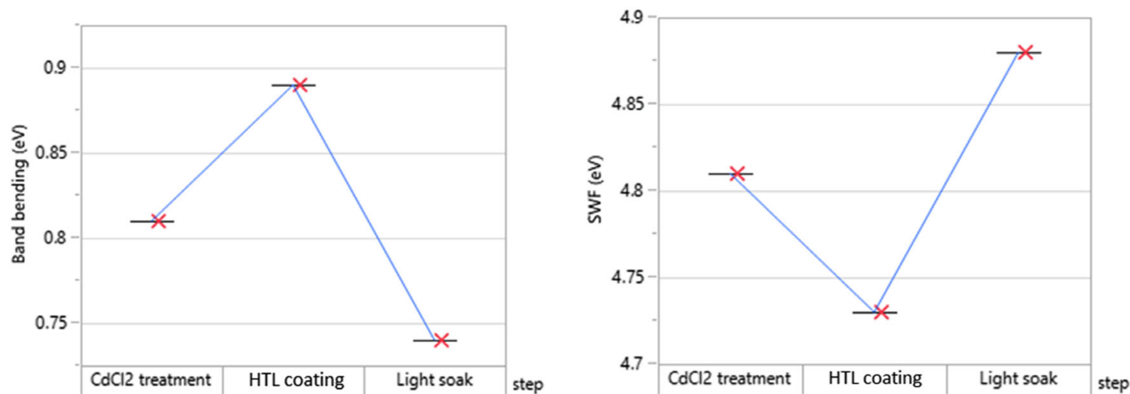

Figure 4. Progress of absorber surface band bending and surface work function measured by Kelvin probe. Process steps are 1) $CdCl_2$ treatment, 2) HTL coating, and 3) light soaking.

© 2023 The Authors. Solar RRL published by Wiley-VCH GmbH

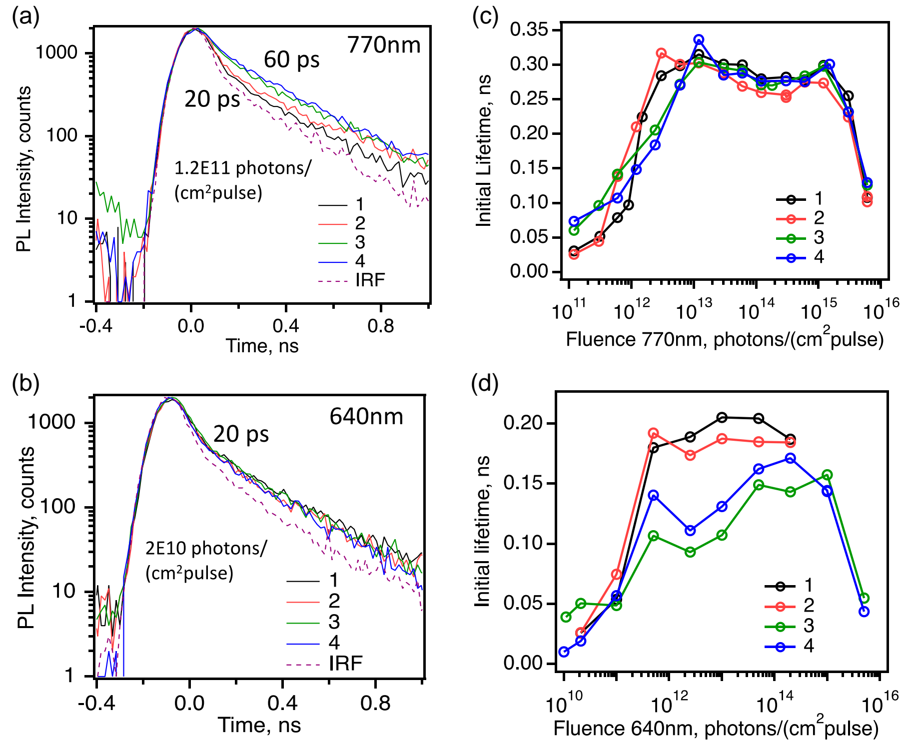

Figure 5. Back-side TRPL data measured with 770 nm (a,c) and 640 nm (b,d) excitation for device stacks 1–4 illustrated in Scheme 1. a,b) show lowest injection TRPL decays. Instrumental response (IRF) used in extracting near-interface lifetimes is shown as a dashed line. c,d) show injection-dependent initial lifetimes measured with c) 770 nm and d) 640 nm excitation.

interface recombination velocity can also have exponential dependence on the interface barrier height.[31] In classical photoconductive decay experiments, nonlinear recombination velocity dependence on interface charges was found for Si/SiO_2 interfaces (rates both increasing and decreasing with defect density).[32] Using defect models requires assumptions about interface defect energies, densities, and capture cross-sections, and this information is not available for CdTe. We analyze relatively "simpler" cases where carrier dynamics after pulsed (300 fs) excitation is very fast (20–60 ps) and a linear response model seems appropriate. Device simulations (Section 2.4) support using this approximation and suggest that a Equation (4) can be useful for the analysis of other thin-film interfaces with high recombination rates.

We first consider the lowest injection data in Figure 5a ($\lambda_{ex} = 770$ nm) and b ($\lambda_{ex} = 640$ nm). Fast dynamics ($\tau_1 = 20$–60 ps) indicate strong space charge field, in agreement with large band bending determined from XPS and Kelvin probe. Using the first term in Equation (4), initial rate $1/\tau_1 = (1.7-5) \times 10^{10}\ s^{-1}$ indicates $\mu E \approx (0.7-4) \times 10^6\ cm\ s^{-1}$. The field strength is related to the built-in voltage φ_{bi}: $E = 2\varphi_{bi}/w_d$. Using $w_d \approx 0.2\ \mu m$, $\mu\varphi_{bi} \approx 7$–$40\ cm^2\ s^{-1}$. Separating μ and φ_{bi} requires assumptions about mobility. Charge carrier mobility in large grain undoped CdSeTe can be as high as $\mu \approx 100\ cm^2\ (Vs)^{-1}$,[8] but mobility can be reduced due to impurity scattering. For example, in As-doped single crystal CdTe, unactivated As (As_{Te} activation in devices studied here $\leq 2\%$)[10,11] was suggested to reduce charge carrier mobility from 800 to 10–40 $cm^2\ (Vs)^{-1}$.[33] Using the value from the middle of this range, $\mu = 20\ cm^2\ (Vs)^{-1}$, estimated $\varphi_{bi} \geq 0.35$ V is consistent with the surface analysis results (Table 1).

The electrostatic model can relate φ_{bi} to the density of charged interface defects N_S^+

$$\varphi_{bi} = \frac{qN_S^{+2}}{2\varepsilon_0\varepsilon_s(p+n)} \tag{5}$$

where ε_0 is vacuum permittivity, ε_s is static dielectric constant, and n is photoinjected carrier density. At the lowest injection $p >> n$, and $N_S^+ \geq 2.8 \times 10^{11}\ cm^{-2}$ corresponds to $\varphi_{bi} \geq 0.35$ V. As shown in Section 2.4, N_S^+ is about an order magnitude larger than the neutral defect density N_S, and interface charges have larger impact than neutral recombination centers.

2.4. Modeling Charge Carrier Dynamics and Device Characteristics

We apply numerical modeling to analyze TRPL data (Figure 5) without simplifications of the analytical model (Equation (4)). This analysis verifies rate interpretation in terms of neutral and charged recombination center defect densities, N_S and N_S^+. TRPL simulations also narrow down parameters required for device current–voltage analysis, described next. Section 4.5 provides details regarding methodology. Device parameter values used in simulations are listed in Table S2 and S3, Supporting Information.

© 2023 The Authors. Solar RRL published by Wiley-VCH GmbH

2367198x, 2023, 10, Downloaded from https://onlinelibrary.wiley.com/doi/10.1002/solr.202300073 by National Renewable Energy Lab, Wiley Online Library on [01/06/2023]. See the Terms and Conditions (https://onlinelibrary.wiley.com/terms-and-conditions) on Wiley Online Library for rules of use; OA articles are governed by the applicable Creative Commons License

2367198x, 2023, 10, Downloaded from https://onlinelibrary.wiley.com/doi/10.1002/solr.202300073 by National Renewable Energy Lab, Wiley Online Library on [01/06/2023]. See the Terms and Conditions (https://onlinelibrary.wiley.com/terms-and-conditions) on Wiley Online Library for rules of use; OA articles are governed by the applicable Creative Commons License

Figure 6a compares TRPL simulations (solid lines) to estimates from Equation (4) for τ_1 as a function of excitation fluence for $\lambda_{ex} = 640$ and 770 nm. BC properties used here are N_s^+ 3×10^{11} cm^{-2} and $S_{back} = 3 \times 10^4$ cm s^{-1}. To derive initial lifetimes τ_1 from simulations, the first 25 ps of the simulated TRPL decay was fit using an exponential function (see Figure S3, Supporting Information). Trends for simulations and analytical model are similar, as indicated by the three shaded areas. In the low-fluence region drift dominates, and both Equation (4) and numerical model indicate $\tau_1 \approx 25$ ps ($\lambda_{ex} = 640$ nm) and $\tau_1 \approx 60$ ps ($\lambda_{ex} = 770$ nm), in excellent agreement with the experimental data (Figure 5). A mid-power region indicates conditions when the electric field is screened and τ_1 is governed by surface recombination and diffusion, and a high-injection region where radiative recombination supersedes other mechanisms.

Device modeling provides detailed insights into carrier dynamics and solar cell operation. In the drift regime, electron and hole transport are both important during the first 100 ps. This is evident in Figure 6b where the quasi-Fermi levels vary significantly within 100 ps of excitation when the electric field is not screened at low fluence. Therefore, a reduced mobility $\mu = \mu_n\mu_p/(\mu_n + \mu_p) = 4.4$ cm^2 (Vs)$^{-1}$ with $\mu_n = 40$ cm^2 (Vs)$^{-1}$ and $\mu_p = 5$ cm^2 (Vs)$^{-1}$ was used in Equation (4).

The drift term depends on injection due to the screening effect. While the peak electric field (E_{max}, at the interface) remains unchanged with fluence, the screening length varies considerably. At low injection, the field decays linearly over the depletion width, $w_d \approx 160$ nm for $N_A = 2 \times 10^{16}$ cm^{-3}. In that case, the mean field is roughly $E_{max}/2$. In Figure 6a, it can be seen that significant field screening occurs when the fluence surpasses the surface charge density ($N_s^+ = 3 \times 10^{11}$ cm^{-2}), providing a simple visual estimate of N_s^+. At higher injection, the field decays exponentially over the Debye length, L_D. Drift becomes insignificant when the absorption depth is greater than L_D.

In the mid-power range, there is an interplay of interface recombination and diffusion. Using model values in the interface recombination term [cf. Equation (4)], yields $\tau_{back} = 1/(2\alpha S_{back}) = 125$ and 250 ps for $\lambda_{ex} = 640$ and 770 nm, respectively. Although the model results double from $\lambda = 640$ to 770 nm, as expected due to the doubling of $1/\alpha$, the magnitudes at the mid-power range are lower at approximately 100 and 200 ps (Figure 6a). The reason for the discrepancy is that the diffusion times within the length $1/\alpha$ are $\tau_{diff} = 500$ and 1000 ps for $\lambda = 640$ and 770 nm, respectively, resulting in the simulated $\tau_1 = (\tau_{diff}^{-1} + \tau_{back}^{-1})^{-1} = 100$ and 200 ps. Hence, the simulations suggest that diffusion contributes slightly to the τ_1 value in the mid-power range.

Radiative lifetime dominates in the high injection case and is given by $\tau_{rad} = 1/Bn$, where B is the radiative recombination coefficient and n is the electron density within $1/\alpha$ of the interface. With $B = 10^{-10}$ cm^3 s^{-1}, Figure 6a shows that radiative recombination starts to affect τ_1 at fluence $>10^{14}$ photons pulse^{-1} cm^{-2}, above which τ_1 rapidly decreases. The data indicates the transition to the radiative regime closer to 10^{15} photons pulse^{-1} cm^{-2}. That discrepancy may be due to the value of B used in the models.

Overall, the simulations support the predictions of Equation (4) and exhibit the same trends as the data, but it is important to note that precise correspondence is not the goal. Discrepancies arise due to the lack of numerical factors in Equation (4) and uncertainties in the parameter values used in the device simulations. Selecting physically meaningful τ_1 values from the early time TRPL simulations to compare with the data is another source of uncertainty. In this work, the first 25 ps was considered representative because it is slightly greater than instrument response function of 20 ps and within the range of the expected drift time based on the data (Figure 4). Despite the uncertainties, we note that order of magnitude estimates can be obtained.

Figure 7 compares JV data to simulations for a completed device with metal BC. A detailed list of parameter values is

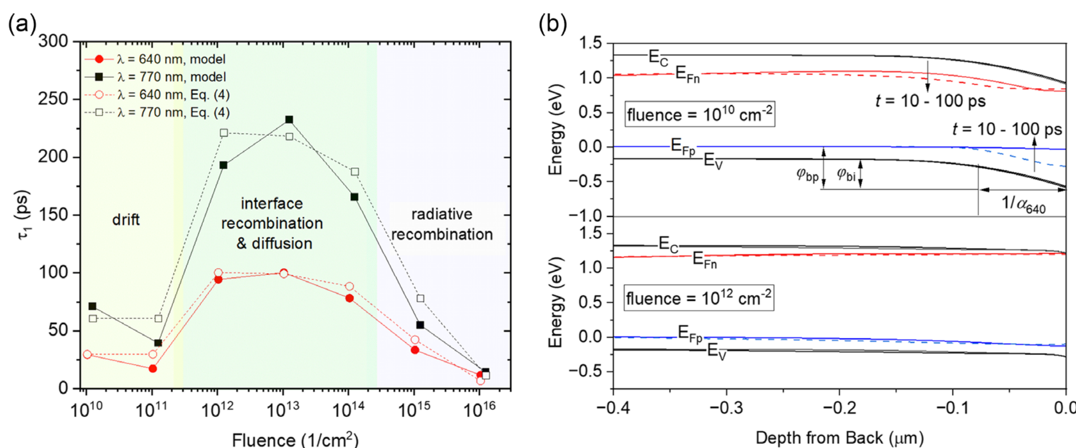

Figure 6. a) Early TRPL τ_1 as a function of laser fluence for excitation wavelengths 640 nm (circles) and 770 nm (squares). Numerical simulations (filled symbols, solid lines are guides to the eye) are compared with the analytical estimates of Equation (4) (open symbols and dashed lines). Shaded regions indicate dominant mechanisms. b) Energy levels near the back surface at $t = 10$ ps (solid) and 100 ps (dashed) after excitation with fluence 10^{10} photons pulse^{-1} cm^{-2} (top) and 10^{12} photons pulse^{-1} cm^{-2} (bottom) when $\lambda_{ex} = 640$ nm. Top panel indicates built-in potential, φ_{bi}, hole back barrier, φ_{bp}, and absorption depth, $1/\alpha_{640}$, when the electric field is not screened at lower fluence.

 © 2023 The Authors. Solar RRL published by Wiley-VCH GmbH

2367198x, 2023, 10, Downloaded from https://onlinelibrary.wiley.com/doi/10.1002/solr.202300073 by National Renewable Energy Lab, Wiley Online Library on [01/06/2023]. See the Terms and Conditions (https://onlinelibrary.wiley.com/terms-and-conditions) on Wiley Online Library for rules of use; OA articles are governed by the applicable Creative Commons License

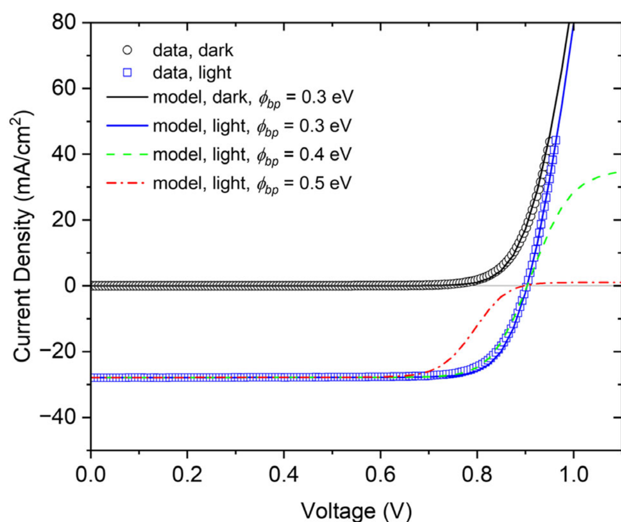

Figure 7. Device simulations using parameters in Table S2 and S3, Supporting Information, when the back barrier is varied. Dark and 1-sun light JV data (points) and simulations showing the effects of back barrier heights 0.3 eV (solid lines), 0.4 eV (dashed), and 0.5 eV (dash-dot).

provided in Table S2 and S3, Supporting Information. Key parameters of note here are the bulk minority carrier lifetime, τ_n, front SRV (i.e., at the buffer/Cd(Se,Te) interface), S_{front}, back SRV, S_{back}, back barrier height, φ_{bp}, and electron and hole mobilities, μ_n and μ_p. Based on the mid-power TRPL results shown in Figure 1c, a value of $\tau_n = 100$ ns was used. Given that value, V_{oc} is mostly determined by and sensitive to front SRV and a value of $S_{front} = 3 \times 10^3\ cm\ s^{-1}$ fit the data closely. The models also included $S_{back} = 10^5\ cm\ s^{-1}$, consistent with the estimates in Section 2.3. In this case, V_{oc} is rather insensitive to S_{back}. In contrast, band bending has much larger effect on solar cell efficiency. We consider the impact of band bending in several simulations in Figure 7. First, for $\varphi_{bp} = 0.4$ and 0.5 eV the barrier is too high to account for forward current ($V > V_{oc}$), as exhibited by the JV curve rollover. The simulation with $\varphi_{bp} = 0.3$ V is in good agreement with experimental JV (Section 4). This suggests that the addition of a metal BC on the completed device lowers that barrier to <0.35 eV or lateral nonuniformity in barrier height creates low barrier pathways. The thin, highly *p*-doped ZnTe could create a thin enough barrier to allow tunneling, thereby reducing the effect of the barrier. Mobilities of 40 and 5 $cm^2\ Vs^{-1}$ for electrons and holes, respectively, are consistent with the JV data except for small discrepancies in the fill factor that could be accounted for by slightly lowering the mobilities in the models.

3. Conclusion

BC losses can limit external radiative efficiency and device voltage of CdTe solar cells. By using surface analysis (XPS and Kelvin probe) and electro-optical (time- and spectrally-resolved PL) techniques, we quantified the impact of interface recombination and interface barrier. Results were integrated into a solar cell device model. As a model system, we analyzed sequential fabrication of BC stack and showed how defect density changes in the fabrication process. We find that charged interface defect density N_S^+ is approximately an order of magnitude higher than the neutral SRH recombination center defect density N_S, and as a result near-BC band bending is more detrimental to the device than BC recombination.

Analysis indicates that both interface defects (N_S) and interface charges (N_S^+) need to be reduced to improve the performance of CdTe solar cells. For device stacks in this study interface charges are more detrimental, and HTL device architecture considered here did not reduce interface charges sufficiently. Recent computational search suggested additional BC materials for consideration.[34]

4. Experimental Section

Solar Cell Fabrication and Characterization: Fabrication of bilayer CdSeTe/CdTe solar cells doped with As was described by Metzger et al.[10] with additional details given in refs. [18] and [15]. Application of poly[bis(4-phenyl)(2,4,6-trimethylphenyl)amine (PTAA) HTL to CdTe device stack by spin coating was described by Hack et al.[14] ZnTe:N (100 nm on silicon) for determination of ZnTe valence band to core level energy was obtained from First Solar. To make back interface accessible for characterization, EO and surface analysis are applied to incomplete device stacks in Scheme 1, with focus on understanding changes with HTL. In complete devices, carrier density determined with capacitance-voltage (CV) is $p = 2 \times 10^{16}\ cm^{-3}$. In **Figure 8**, current voltage (JV) and EQE of the finished device show 20.1% device efficiency with 902 mV open circuit voltage and 27.9 $mA\ cm^{-2}$ short circuit current. The short circuit current has been calibrated by EQE. The device stack is CdSeTe/CdTe bilayer followed by HTL, ZnTe, and back metal. The optimization of an absorber surface treatment, HTL coating, the front and BC layers, and doping level is critical to achieve high performance with a good open circuit voltage. Characterization measurements were applied to three sample sets.

Photoluminescence Spectroscopy: PL emission spectra were measured with excitation at 632.8 nm (HeNe laser) using HRS-300 spectrometer (Princeton Instruments) equipped with Si and InGaAs detectors. Detector spectral responses were calibrated using manufacturer-provided visible and near-IR intensity calibration sources and placing them in the sample position. Absolute PL emission intensities were determined using 2% and 5% reflectance standards (LabSphere). Excitation intensity was varied from 7 to 61 $mW\ cm^{-2}$, which corresponds to 0.12–1 Sun equivalent photon fluence for the $E_g = 1.4$ eV bandgap. We used time-resolved PL (TRPL) measurements with excitation through glass (front junction) and from the back of the absorber stack. Excitation was at 640 or 770 nm (300 fs pulses at 0.2–1.1 MHz repetition rate) and PL emission was measured with 800–840 nm bandpass filter. Time-correlated single photon counting (with Picoharp 300 from Picoquant) and avalanche photodiode (PDM with integrated multimode optical fiber from Micro Photon Devices) was used for detection. Excitation fluence was varied from the lowest where data can be obtained and increased until lifetimes became shorter due to radiative recombination at high injection; this fluence range establishes conditions for SRH recombination analysis.

X-Ray Photoelectron Spectroscopy (XPS): XPS measurements were performed in a Physical Electronics VersaProbe III using monochromatic Al K_α radiation. Samples were examined without light-soaking treatment and in open circuit conditions. High energy resolution core level and valence band spectra for band position determination were acquired at a near-normal electron take-off angle and with a pass energy of 27 eV. Wide range, low energy resolution survey spectra to quantify surface composition were performed with a pass energy of 280 eV. To assess X-ray-induced photovoltages, Cd $3d_{5/2}$ and Te $3d_{5/2}$ spectra were taken

 © 2023 The Authors. Solar RRL published by Wiley-VCH GmbH

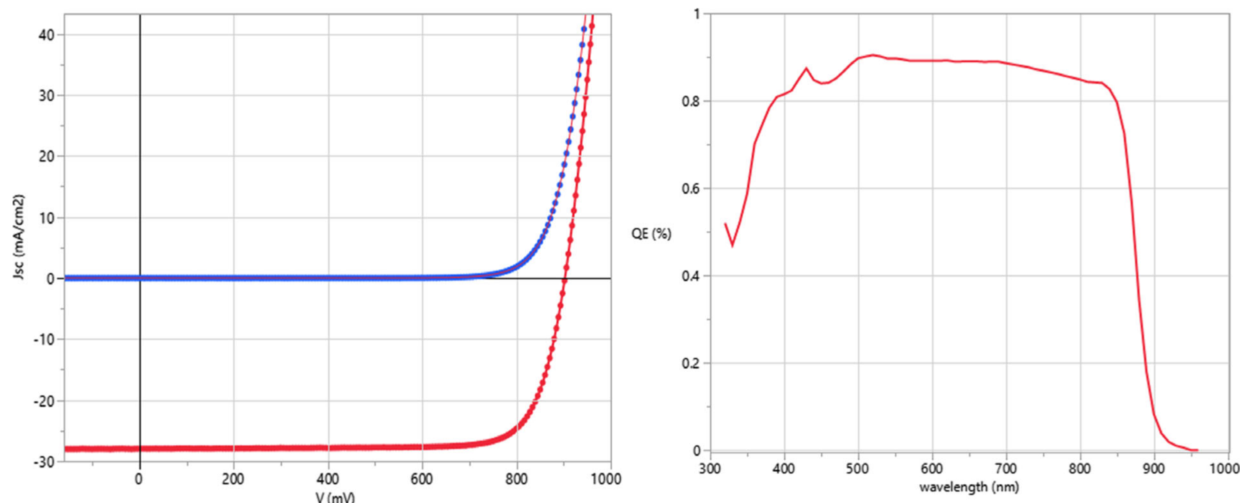

Figure 8. Experimental JV (left) and EQE (right) characteristics of bilayer CdSeTe/CdTe solar cell where metal stack is applied to complete HTL/ZnTe stack 1 (Scheme 1).

at high and low intensity (15 μm spot, 2.4 W anode and 100 μm spot, 24 W anode, respectively). The instrument binding energy scale was calibrated using the Fermi edge feature at 0 eV and Au $4f_{7/2}$ and Cu $2p_{3/2}$ peaks of sputter-cleaned foils which were taken to be 83.98 and 932.67 eV, respectively. Core level to valence band maxima energy differences were determined using spectra from materials that had been cleaned in situ using a gas cluster ion source (10 kV, Ar_{2000}^{+}). These energy differences were then used to determine valence band maxima in films in "as-received" condition, that is, without any cleaning and with air exposure, ensuring the same surface condition as for films examined with surface photovoltage and PL. Valence band maxima were located by two methods which were found to be self-consistent: 1) extrapolation of the linear portion of the VBM to the background at lower binding energy26 and 2) by fitting XPS data to theoretical total density of states (DOS).[35]

Kelvin Probe/Surface Photovoltage: Kelvin probe and surface photovoltage measurements were performed with a KP020 Kelvin probe by KP Technology with an add-on light source (KP Technology SPV020). The surface band bending has been extracted by calculating the difference between a measured surface work function and a bulk work function. The bulk work function was estimated to be 5.62 eV with 5.8 eV valence band edge, 1.5 eV bandgap, and 2×10^{16} cm^{-3} doping level.

Device Modeling: Numerical calculations were employed to solve the coupled Poisson and time-dependent charge continuity equations using the finite volume method. Simulations were performed using COMSOL Multiphysics software v6.0. Device models consisted of a 1D stack with Ohmic front contact/n-SnO_2 (300 nm)/buffer (50 nm)/*p*-Cd(Se,Te) (3,000 nm) with a free back surface. A Schottky-type BC was added to simulate JV. Parameter values used in simulations are provided in Table S2, Supporting Information, and were based on Refs. [24] and [36]. Fermi-Dirac statistics were employed to account for the high doping levels in SnO_2. The doped SnO_2:F transparent conducting oxide was assumed to be part of the Ohmic contact. The $CdSe_yTe_{1-y}$ layer had $y = 0.30$ near the buffer with an erfc(x) grading over about 1 μm down to pure CdTe. The Cd(Se,Te) electron affinity and band gap were graded in response to the Se profile.[37] Properties of the free back surface included surface recombination velocity, S_{back}, and surface charge density, N_s^+. Nonradiative recombination and defect charge at the back surface were decoupled for simplicity such that defect energy distribution was not a factor.

Device modeling was applied to simulate device performance (current–voltage) and TRPL. TRPL excitation was implemented using a similar approach as Reference.[24] A Gaussian pulse of light intensity over time was centered at 3 ps with an FWHM of 0.35 ps. Exponentially decaying light absorption within the Cd(Se,Te) layer was assumed according to the absorption coefficient $\alpha = A\sqrt{h\upsilon - E_g}$ with $A = 2 \times 10^5$ cm^{-1} eV$^{-1/2}$. The PL intensity as a function of time was calculated as the integral of the radiative recombination rate over the Cd(Se,Te) layer. Multiple internal reflections and photon recycling were not included.

Supporting Information

Supporting Information is available from the Wiley Online Library or from the author.

Acknowledgements

This work was authored in part by the National Renewable Energy Laboratory, operated by Alliance for Sustainable Energy, LLC, for the U.S. Department of Energy (DOE) under Contract No. DE-AC36-08GO28308. The views expressed in the article do not necessarily represent the views of the DOE or the U.S. Government. This article has been contributed to by US Government contractors and their work is in the public domain in the USA. This material is based upon work supported by the U.S. Department of Energy's Office of Energy Efficiency and Renewable Energy (EERE) under the Solar Energy Technology Office (SETO) Award Numbers 8974 and 38525.

Conflict of Interest

The authors declare no conflict of interest.

Data Availability Statement

The data that support the findings of this study are available from the corresponding author upon reasonable request.

Keywords

characterization, charge carrier lifetime, contacts, device modeling, photoluminescence, thin film solar cells, X-ray photoelectron spectroscopy

© 2023 The Authors. Solar RRL published by Wiley-VCH GmbH

2367198x, 2023, 10, Downloaded from https://onlinelibrary.wiley.com/doi/10.1002/solr.202300073 by National Renewable Energy Lab, Wiley Online Library on [01/06/2023]. See the Terms and Conditions (https://onlinelibrary.wiley.com/terms-and-conditions) on Wiley Online Library for rules of use; OA articles are governed by the applicable Creative Commons License

Received: January 31, 2023
Revised: February 23, 2023
Published online: March 12, 2023

[1] T. Song, A. Moore, J. R. Sites, *IEEE J. Photovolt.* **2018**, *8*, 293.
[2] G. K. Liyanage, A. B. Phillips, F. K. Alfadhili, R. J. Ellingson, M. J. Heben, *ACS Appl. Energy Mater.* **2019**, *2*, 5419.
[3] D. Kuciauskas, A. Kanevce, J. M. Burst, J. N. Duenow, R. Dhere, D. S. Albin, D. H. Levi, R. K. Ahrenkiel, *IEEE J. Photovolt.* **2013**, *3*, 1319.
[4] T. P. Weiss, B. Bissig, T. Feurer, R. Carron, S. Buecheler, A. N. Tiwari, *Sci. Rep.* **2019**, *9*, 5385.
[5] A. Onno, C. Chen, P. Koswatta, M. Boccard, Z. C. Holman, *J. Appl. Phys.* **2019**, *126*, 183103.
[6] H. M. Wikoff, S. B. Reese, M. O. Reese, *Joule* **2022**, *6*, 1710.
[7] M. Amarasinghe, D. Albin, D. Kuciauskas, J. Moseley, C. L. Perkins, W. K. Metzger, *Appl. Phys. Lett.* **2021**, *118*, 211102.
[8] D. Kuciauskas, J. Moseley, P. Ščajev, D. Albin, *Phys. Status Solidi RRL* **2020**, *14*, 1900606.
[9] A. R. Duggal, J. J. Shiang, W. H. Huber, A. F. Halverson, US 20140373908A1, **2013**.
[10] W. K. Metzger, S. Grover, D. Lu, E. Colegrove, J. Moseley, C. L. Perkins, X. Li, R. Mallick, W. Zhang, R. Malik, J. Kephart, C.-S. Jiang, D. Kuciauskas, D. S. Albin, M. M. Al-Jassim, G. Xiong, M. Gloeckler, *Nat. Energy* **2019**, *4*, 837.
[11] E. Colegrove, B. Good, A. Abbas, H. Moutinho, S. Johnston, C.-S. Jiang, P. O'Keefe, J. M. Walls, D. S. Albin, M. O. Reese, *Sol. Energy Mater. Sol. Cells* **2022**, *246*, 111886.
[12] D. Krasikov, D. Guo, S. Demtsu, I. Sankin, *Sol. Energy Mater. Sol. Cells* **2021**, *224*, 111012.
[13] D. Kuciauskas, J. M. Kephart, J. Moseley, W. K. Metzger, W. S. Sampath, P. Dippo, *Appl. Phys. Lett.* **2018**, *112*, 263901.
[14] J. Hack, C. Lee, S. Grover, G. Xiong, in *IEEE 48th Photovolt. Spec. Conf.*, IEEE, Piscataway, NJ **2021**, pp. 1880–1882.
[15] W. K. Metzger, D. W. Miller, R. Mallick, X. Li, W. Zhang, I. Wang, A. Polizzotti, T. Ablekim, D. H. Cao, D. C. Hamilton, J. Bailey, C. Lee, S. Grover, D. Lu, G. Xiong, *IEEE Journal of Photovoltaics* **2022**, *12*, 1435.
[16] D. Kuciauskas, P. Dippo, Z. Zhao, L. Cheng, A. Kanevce, W. K. Metzger, M. Gloeckler, *IEEE J. Photovoltaics* **2016**, *6*, 313.
[17] D. Kuciauskas, J. Moseley, C. Lee, *Sol. RRL* **2021**, *5*, 2000775.
[18] A. Onno, C. Reich, S. Li, A. Danielson, W. Weigand, A. Bothwell, S. Grover, J. Bailey, G. Xiong, D. Kuciauskas, W. Sampath, Z. C. Holman, *Nat. Energy* **2022**, *7*, 400.
[19] J. Moseley, S. Grover, D. Lu, G. Xiong, H. L. Guthrey, M. M. Al-Jassim, W. K. Metzger, *J. Appl. Phys.* **2020**, *128*, 103105.
[20] V. Sarritzu, N. Sestu, D. Marongiu, X. Chang, S. Masi, A. Rizzo, S. Colella, F. Quochi, M. Saba, A. Mura, G. Bongiovanni, *Sci. Rep.* **2017**, *7*, 44629.
[21] T. Unold, L. Gütay in *Solar Cells*, (Eds: D. Abou-Ras, T. Kirchartz, U. Rau) 2nd ed., Wiley- VCH, Weinheim **2016**, pp. 275–297.
[22] M. H. Wolter, R. Carron, E. Avancini, B. Bissig, T. P. Weiss, S. Nishiwaki, T. Feurer, S. Buecheler, P. Jackson, W. Witte, S. Siebentritt, *Progr. Photovolt.* **2022**, *30*, 702.
[23] A. Onno, S. Li, C. Reich, A. Danielson, W. Weigand, W. Sampath, D. Kuciauskas, Z. C. Holman, in *IEEE 48th Photovolt. Spec. Conf.*, IEEE, Piscataway, NJ **2021**, pp. 1754–1757..
[24] J. Moseley, D. Krasikov, C. Lee, D. Kuciauskas, *J. Appl. Phys.* **2021**, *130*, 163105.
[25] J. Moseley, D. Krasikov, D. Kuciauskas, in *48th Photovolt. Spec. Conf.*, IEEE, Piscataway, NJ **2021**, pp. 1687–1690.
[26] S. A. Chambers, T. Droubay, T. C. Kaspar, M. Gutowski, M. Van Schilfgaarde, *Surf. Sci.* **2004**, *554*, 81.
[27] C. H. Swartz, E. G. LeBlanc, C. Perkins, D. L. McGott, M. O. Reese, A. Nichols, T. H. Myers, *Appl. Surf. Sci.* **2022**, *598*, 153656.
[28] B. Späth, J. Fritsche, A. Klein, W. Jaegermann, *Mater. Res. Soc. Symp. Proc.* **2004**, *865*(.
[29] A. Klein, *J. Phys. Condens. Matter* **2015**, *27*, 134201.
[30] M. Maiberg, C. Spindler, E. Jarzembowski, R. Scheer, *Thin Solid Films* **2015**, *582*, 379.
[31] F. Cadiz, D. Paget, A. C. H. Rowe, V. L. Berkovits, V. P. Ulin, S. Arscott, E. Peytavit, *J. Appl. Phys.* **2013**, *114*, 103711.
[32] A. W. Stephens, A. G. Aberle, M. A. Green, *J. Appl. Phys.* **1994**, *76*, 363.
[33] P. Ščajev, A. Mekys, L. Subačius, S. Stanionytė, D. Kuciauskas, K. G. Lynn, S. K. Swain, *Sci. Rep.* **2022**, *12*, 12851.
[34] P. Gorai, D. Krasikov, S. Grover, G. Xiong, W. K. Metzger, V. Stepanovic, *ChemRxiv* **2022**, https://doi.org/10.26434/chemrxiv-2022-lpb63.
[35] E. A. Kraut, R. W. Grant, J. R. Waldrop, S. P. Kowalczyk, *Phys. Rev. B* **1983**, *28*, 1965.
[36] A. Kanevce, M. O. Reese, T. M. Barnes, S. A. Jensen, W. K. Metzger, *J. Appl. Phys.* **2017**, *121*, 214506.
[37] J. Yang, S.-H. Wei, *Chinese Phys. B* **2019**, *28*, 086106.

© 2023 The Authors. Solar RRL published by Wiley-VCH GmbH

2367198x, 2023, 10, Downloaded from https://onlinelibrary.wiley.com/doi/10.1002/solr.202300073 by National Renewable Energy Lab, Wiley Online Library on [01/06/2023]. See the Terms and Conditions (https://onlinelibrary.wiley.com/terms-and-conditions) on Wiley Online Library for rules of use; OA articles are governed by the applicable Creative Commons License